

**Ionization suppression of Cl<sub>2</sub> molecules in intense laser fields**

E. P. Benis,\* J. F. Xia, X. M. Tong, M. Faheem, M. Zamkov, B. Shan, P. Richard, and Z. Chang  
*J. R. Macdonald Laboratory, Department of Physics, Kansas State University, Manhattan, Kansas 66506-2604, USA*  
 (Received 30 October 2003; published 26 August 2004)

The strong field ionization of Cl<sub>2</sub> molecules is investigated by using an ultrashort pulse Ti:sapphire laser. A spatial imaging technique is used in such measurements to reduce the effect of spatial integration. Cl<sub>2</sub> shows strong ionization suppression as do other diatomic molecules having valence orbitals with antibonding symmetry (O<sub>2</sub>, S<sub>2</sub>) when compared with the field ionization of atoms with nearly identical ionization potential. A more general molecular tunneling ionization model is proposed, and the calculations are in reasonable agreement with the measurements. Our results support that antibonding leads to ionization suppression, a trend that only F<sub>2</sub> goes against and that needs to be further investigated.

DOI: 10.1103/PhysRevA.70.025401

PACS number(s): 33.80.Rv, 32.80.Rm, 34.50.Gb, 42.50.Hz

Perhaps the most fundamental process in the interaction of strong laser fields with molecules is single electron ionization. Even though atomic ionization has been extensively investigated both theoretically and experimentally, the study of molecular ionization is still far from complete. Early experimental data [1,2] indicated that the ionization rates of diatomic molecules were similar to atoms with nearly identical ionization potentials (IPs). A simple tunneling ionization model suggested by Perelomov *et al.* [3], and simplified by Ammosov *et al.*, [4] (referred to as the ADK model) were used to explain the atomic tunneling ionization. However, further investigations on diatomic molecules showed that the ionization is strongly suppressed for the cases of D<sub>2</sub> (IP of 15.467 eV) and O<sub>2</sub> (IP of 12.070 eV) in comparison to their companion atoms Ar (IP of 15.764 eV) and Xe (IP of 12.13 eV), respectively, while the ionization rate for N<sub>2</sub> (IP of 15.581 eV) and F<sub>2</sub> (IP of 15.697 eV) is comparable to their companion Ar atom [5–9].

Early theoretical interpretations proposed the mechanisms of molecular alignment [5] and dissociative recombination [6] to explain the suppression in the cases of D<sub>2</sub> and O<sub>2</sub>, respectively. However, they proved to be inadequate by later theoretical [10] and experimental studies [7,11]. A possible effect on ionization suppression from the vibrational motion of the molecules was shown to be too small by Saenz [10]. Guo proposed a larger “effective” ionization potential imposed by a larger effective charge experienced by the open-shell valence electron [12]. However, the proposed model cannot be obtained theoretically or empirically from other experiments and does not account for the behaviors of F<sub>2</sub> and D<sub>2</sub>, as discussed by Wells *et al.* [9]. Muth-Bohm *et al.* [13] explained the ionization suppression in O<sub>2</sub> as the result of destructive interference in the electron emission probability from the two centers. The model fails to explain the suppression of D<sub>2</sub>. Moreover, it predicts suppression for F<sub>2</sub>, a result which contradicts experiment [8,9]. Tong *et al.* [14] developed a molecular ADK (MO-ADK) which is based on the

assumptions of the ADK model for tunneling ionization of atoms, but suitably modified to account for the difference in the electronic wave functions in atoms and molecules. Results from their MO-ADK model are in good agreement with measured ratios of ionization signals for pairs with suppression (D<sub>2</sub>:Ar, O<sub>2</sub>:Xe) and pairs without suppression (N<sub>2</sub>:Ar, CO:Kr). Results are also in agreement with the measured ionization signals of NO, S<sub>2</sub>, and SO. However, the model predicts suppression for F<sub>2</sub>: Ar, which is in disagreement with experiment. Is F<sub>2</sub> an exception to the MO-ADK model or is the MO-ADK model not valid for the full-filled antibond orbital?

To answer the question, in this Brief Report, we present a measurement of the field ionization of Cl<sub>2</sub> (IP of 11.48 eV), which has a full-filled antibond orbital, in comparison to its closest companion atom, Xe. A spatial imaging technique was used to measure the ionization of mixed Cl<sub>2</sub> and Xe gas target. The basic advantage of the technique is that the ionization signal can be obtained at one laser pulse energy. A more general molecular tunneling ionization model is proposed and calculations are compared to the measurements. So far, only O<sub>2</sub> and S<sub>2</sub> showed strong suppression predicted by the MO-ADK model, leaving F<sub>2</sub> as a puzzling exception. By including Cl<sub>2</sub> in the single ionization suppression studies we expect to shed more light on the issue.

The experiments were performed at the J. R. Macdonald Laboratory at Kansas State University using the Kansas Light Source (KLS), i.e., a Ti:sapphire laser delivering 790 nm, 25 fs pulses with an energy of 4 mJ at a repetition rate of 1 kHz. A beam splitter for ultrafast optics has been used to pick up ~20% of the the total output to this experiment. The on-target laser power was tuned by a variable neutral density filter. The linearly polarized pulses were focused by a 25 cm focal length lens into the UHV chamber. The UHV chamber maintained a base pressure of  $2 \times 10^{-9}$  Torr. A mixture of equal pressures of the two gases (Cl<sub>2</sub> and Xe) was prepared in a small volume bottle and then introduced into the chamber through the needle valve, reaching pressures up to  $1 \times 10^{-5}$  Torr. Special care was taken in order to minimize any side effects caused by the increased reactivity of Cl<sub>2</sub> with H<sub>2</sub>O and other contaminants in the vacuum chamber. A residual gas analyzer was utilized to

\*Present address: Institute of Electronic Structure and Laser, P.O. Box 1527, 71110, Heraklion, Crete, Greece; electronic address: benis@iesl.forth.gr

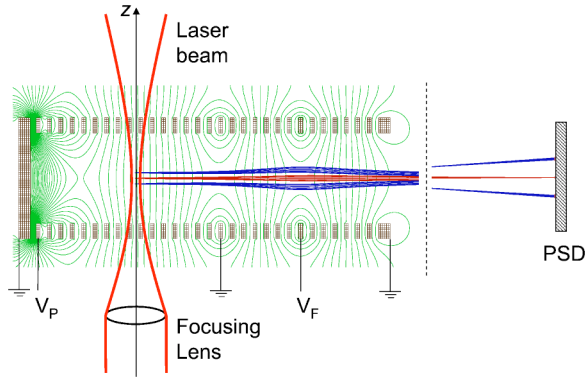


FIG. 1. Schematic setup of the imaging spectrometer. A side cut of the SIMION three-dimensional model showing the electrodes, the equipotential lines, and parts of the paths of three different groups of ions created along the beam propagation axis and imaged on a position sensitive detector (PSD) are illustrated.

monitor the ratio of  $(\text{Xe}^{2+} + \text{Xe}^+)/(\text{Cl}_2^+ + \text{Cl}^+)$ , showing fair stability for a period of time large enough compared to the experiment duration. The use of a dual gas target of a well-known pressure ratio reduces substantially the systematic uncertainties arising from the absolute determination of each gas target partial pressure, and from changes in the laser intensity and alignment [8].

The use of a dual gas target was combined with a spatial-imaging technique according to which the geometrical ionization pattern is reproduced with magnification on a position sensitive detector (PSD). Under ideal imaging conditions there is a one-to-one correspondence between the object and the image. All ions starting from the same point covering a  $4\pi$  emission solid angle are focused at the same point at the detection plane. Thus, the ion yield can be obtained as a function of the laser field intensity since the position information can be straightforwardly related to the corresponding intensity as shown below. To date, strong field ionization has been studied exclusively by measuring the total ion yields while varying the intensity and/or the pressure. While ionization yields are very sensitive to the laser intensity, attempts to minimize the volume effects have been made by extracting the ions through an opening smaller than the confocal length [15]. Volume integration was usually a source of systematic uncertainties. In the imaging technique volume effects are significantly minimized, limited by the quality of the image on the detector. Ideally, a three-dimensional image resolution would lead to the elimination of volume effects. In our case, however, experimental limiting factors in time and position resolution allowed for imaging conditions only along the beam propagation direction. Thus, the ion yield was obtained as a function of the axial peak intensity of the pulse.

As shown in Fig. 1, the laser beam is focused at the axial center of the spectrometer. The spectrometer was used both for extracting and focusing the ions at the detection area. The imaging conditions were studied by means of SIMION simulations. In Fig. 1 a side cut of the SIMION three-dimensional model is shown along the ion extraction plane where the electrodes, the equipotential lines, and parts of the paths of

three different groups of ions created along the beam propagation axis are illustrated. The extracting and focusing regions are electrically connected, forming a pair of thick electrostatic lenses. The ions are emitted isotropically with an energy corresponding to their thermal energy (25 meV). The ion ponderomotive energy is negligible compared to their thermal energy. The extraction and focusing voltages  $V_P$  and  $V_F$ , respectively, were optimized by minimizing the trace width (determined by spherical and chromatic aberrations) at the detection area. The ions are traveling a distance of 1 m after exiting the spectrometer enroute to the detection area. The long distance is essential for increasing the magnification of the object which was measured to be  $M = 6.8$ . A 40 mm two-dimensional PSD with a multihit delay line anode encoder was utilized to record the ion images. A grounded 36% transmission grid was placed in front of the first microchannel plate (MCP) to ensure termination of the MCP fields. Even though we included up to six hits in the detection process, the count rates were kept below one per laser shot to avoid any possible losses of the same specie.

The laser intensity was continually recorded and data corresponding to intensity fluctuations were rejected. The KLS stability is usually within 1%. Special care was taken during the measurements to establish uniform detection efficiencies for different ion species. The MCPs were operated at saturation voltages (1000 V each) and the ratio of  $(\text{Xe}^{2+}/\text{Xe}^+)$  was monitored as a function of the discriminator threshold. The threshold was set at low enough limits within the ratio constancy region to ensure its reliability. The projection of the image along the beam axis determined the resolution at the detector to be 0.93 mm at FWHM. Typical detection images are shown in Fig. 2. The reduction of the raw data was based on the assumption of a Gaussian beam distribution. Thus, the intensity expressed in cylindrical coordinates is written as  $I(r=0, z) = I_0/[1 + (z/z_R)^2]$ , where  $z_R$  is the Rayleigh range,  $I_0$  is the intensity at  $r=0$  and  $z=0$ . The Rayleigh range was estimated to be 1.6 mm. Also, FROG measurement showed that the pulse duration inside the chamber was 44 fs. As already mentioned, the imaging conditions could only be applied along the laser beam direction and therefore the counts were integrated along the other two dimensions. Thus, we performed a  $z$ -scan measurement. The distance  $z$  was estimated after dividing the distance of the image measured on the detector by the magnification factor  $M$ .

Experimentally, the total ionization yield is a final result of volume integration. Traditionally, the experimental results are always confused by volume effects, which blur the physical details. However, since the imaging experiments provide the ionization yield along the laser propagation axis ( $z$ ), we can measure the ionization signal  $S$  at each position  $z$ , thus obtaining the ionization probability  $P(I)$  as a function of the intensity  $I$  as

$$P(I) = \frac{I}{n\pi\Delta z w_0^2 I_0} \frac{d[S(I)]}{d \ln(I_0)}, \quad (1)$$

where  $n$  is the target density,  $\Delta z$  the experimental integration increment along the  $z$  axis, and  $w_0$  the beam waist spot size. The  $S(I)$  is measured from the imaging experiment. An alter-

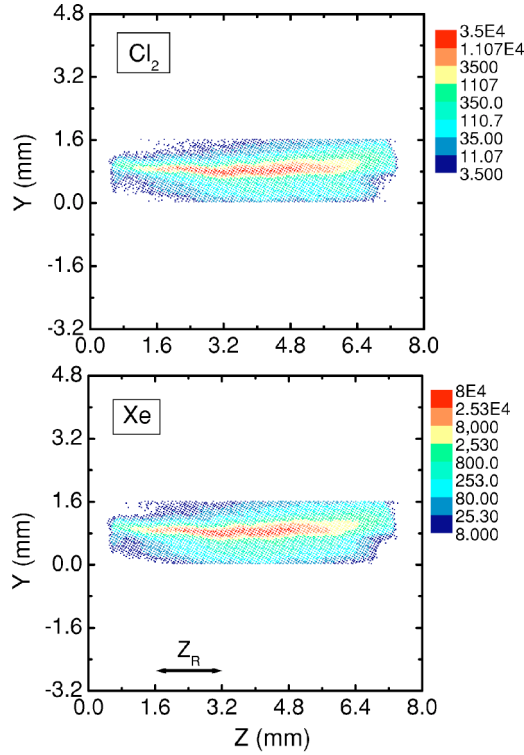


FIG. 2. Typical detection images representing the target area. The  $z$  axis is the laser beam axis while the ion extraction axis points towards the page. The  $Xe^+$  and  $Cl_2^+$  signals were separated in the time-of-flight spectrum by software gates. The laser pulse energy was  $51 \mu J$  while the mixed-gas pressure was kept at  $3 \times 10^{-7}$  Torr.

native way to measure the ionization probability is by measuring the ionization signal from a small slit and then deriving the ionization probability from the measured ionization signal as a function of the peak laser intensity [16]. The basic physical ideas are the same in the two experiments. The advantages of our procedure are: (1) we can measure the  $S(I)$  with one laser power; (2) the measured ionization signal is weighted to the lower intensity, which has a larger interaction area favoring thus statistics.

With this alternative technique, we studied the ionization of  $Cl_2$ . Figure 3 (top) shows our measured ionization signal  $S(I)$  from Xe atoms and  $Cl_2$  molecules. Although the ionization potential of  $Cl_2$  is smaller than that of Xe, the ionization signal of  $Cl_2$  is smaller than that of Xe. This is clear evidence of the strong ionization suppression of  $Cl_2$ .

Before we convert the measured signal to the ionization probabilities from Eq. (1) and compare the result with the tunneling ionization model, we will first discuss the validity region of the tunneling ionization model [4,14]. Based on the Keldysh model [17], the tunneling ionization is valid at  $\gamma = \sqrt{I_p}/2U_p \ll 1$ . For Xe atoms,  $\gamma=1$  when  $I=10^{14} \text{ W/cm}^2$  for 800 nm laser. Our present laser intensity is lower than  $10^{14} \text{ W/cm}^2$  and therefore  $\gamma > 1$ . That means that the tunneling ionization model or ADK model is not valid at this intensity regime. To extend the valid regime of the tunneling ionization to the lower intensity regime, we went back to the original work of Perelomov *et al.* [3] (the PPT model). In the

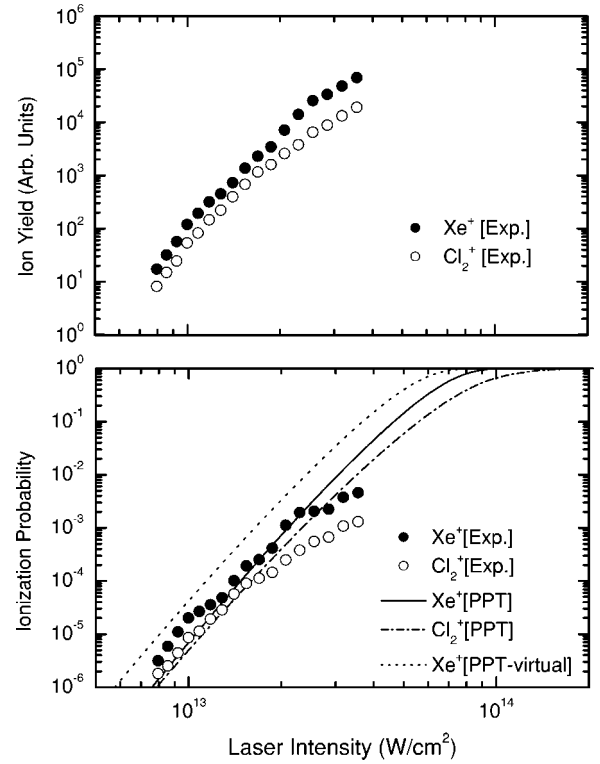


FIG. 3. Single ionization yields for Xe and  $Cl_2$  for linearly polarized laser pulses obtained using the imaging technique. The data correspond to a laser pulse energy of  $51 \mu J$ . Calculations based on the MO-PPT model are shown by curves. The dotted line indicates the ionization probability of a virtual Xe atom with IP of 11.48 eV, i.e., an IP identical to that of  $Cl_2$ . Thus, the strong ionization suppression of  $Cl_2$  becomes evident.

PPT model, the ionization rate of atoms in a lower frequency strong field can be expressed as

$$w(\omega, F) = \frac{B^2(m)}{2^{|m|} |m|!} \frac{A_m(\omega, \gamma)}{\kappa^{2Z_c/\kappa-1}} e^{-2\kappa^3/3Fg(\gamma)} \times \left( \frac{2\kappa^3}{F\sqrt{1+\gamma^2}} \right)^{2Z_c/\kappa-|m|-1}, \quad (2)$$

where  $A_m(\omega, \gamma), g(\gamma)$  are two correction factors to the ADK model, which can be found at Refs. [3,6]. As a matter of fact, the ADK model is a simplified version of PPT. When  $\gamma \rightarrow 0$ , the equation goes back to the ADK rate. To calibrate the valid regime of the ADK and PPT models, we also calculated the ionization probability of Xe by solving the time-dependent Schrödinger equation (TDSE) [18,19]. We calculated the ionization probabilities using TDSE, ADK, and PPT models. The result, although not explicitly shown in this Brief Report due to space limitations, clearly indicates that the PPT model is in better agreement with TDSE calculations, and for a wider range of intensities when compared to the ADK model. We will refer to the PPT model as the molecular PPT, or MO-PPT model.

Figure 3 (bottom) shows our measured ionization probabilities from Eq. (1). A reasonable agreement of the

MO-PPT calculations with the measurements is seen. The observed ionization suppression of  $\text{Cl}_2$  is due to antibond valence orbitals ( $\pi_g$ ) or the geometry of the valence orbital wave function as discussed in Ref. [14]. Note that in lower intensities, the ionization probabilities for Xe and  $\text{Cl}_2$  are close to each other. However, the ionization probability of Xe increases faster than that of  $\text{Cl}_2$  as the laser intensity increases. This is because at lower intensities, the ionization probability is more sensitive to the ionization potential than to the geometry of the wave function. In order to unambiguously observe the ionization suppression, we should compare  $\text{Cl}_2$  with an atom of the same ionization potential, which however, is not available in nature. Instead, in Fig. 3 (bottom), we show the ionization probability for a virtual Xe atom having  $I_p=11.48$  eV. The comparison of the ionization probabilities between  $\text{Cl}_2$  molecule and the corresponding

virtual Xe atom clearly indicates the strong ionization suppression for  $\text{Cl}_2$ .

In conclusion, we developed a spatial imaging technique to measure the ionization probability without convoluting the volume effect. Using this technique, we measured the ionization probabilities of Xe and  $\text{Cl}_2$ . Strong ionization suppression of  $\text{Cl}_2$  was observed. The ionization suppression is attributed to the antibond valence orbital ( $\pi_g$ ) or the geometry of the valence orbital wave function. With this study, we single out the fact that no ionization suppression of  $\text{F}_2$  is an exception to be further investigated.

This work was supported by the Division of Chemical Sciences, Geosciences and Biosciences, Office of Basic Energy Sciences, Office of Science, U.S. Department of Energy. Kansas Light Source was partially funded by a NSF MRI Grant.

- 
- [1] T. D. G. Walsh, J. E. Decker, and S. L. Chin, *J. Phys. B* **26**, L85 (1993).  
[2] T. D. G. Walsh, F. A. Ilkov, J. E. Decker, and S. L. Chin, *J. Phys. B* **27**, 3767 (1994).  
[3] A. M. Perelomov, V. S. Popov, and M. V. Terentev, *Zh. Eksp. Teor. Fiz.* **50**, 1393 (1966) [*Sov. Phys. JETP* **23**, 924 (1966)].  
[4] M. V. Ammosov, N. B. Delone, and V. P. Krainov, *Zh. Eksp. Teor. Fiz.* **91**, 2008 (1986) [*Sov. Phys. JETP* **64**, 1191 (1986)].  
[5] A. Talebpour, C.-Y. Chien, and S. L. Chin, *J. Phys. B* **29**, L677 (1996).  
[6] A. Talebpour, S. Larochelle, and S. L. Chin, *J. Phys. B* **31**, L49 (1998).  
[7] C. Guo, M. Li, J. P. Nibarger, and G. N. Gibson, *Phys. Rev. A* **58**, R4271 (1998).  
[8] M. J. DeWitt, E. Wells, and R. R. Jones, *Phys. Rev. Lett.* **87**, 153001 (2001).  
[9] E. Wells, M. J. DeWitt, and R. R. Jones, *Phys. Rev. A* **66**, 013409 (2002).  
[10] A. Saenz, *J. Phys. B* **33**, 4365 (2000).  
[11] M. Plummer and J. F. MaCann, *J. Phys. B* **30**, L401 (1997).  
[12] C. Guo, *Phys. Rev. Lett.* **85**, 2276 (2000).  
[13] J. Muth-Bohm, A. Becker, and F. H. M. Faisal, *Phys. Rev. Lett.* **85**, 2280 (2000).  
[14] X. M. Tong, Z. X. Zhao, and C. D. Lin, *Phys. Rev. A* **66**, 033402 (2002).  
[15] M. A. Walker, P. Hansch, and L. D. Van Woerkom, *Phys. Rev. A* **57**, R701 (1998).  
[16] S. M. Hankin, D. M. Villeneuve, P. B. Corkum, and D. M. Rayner, *Phys. Rev. A* **64**, 013405 (2001).  
[17] L. V. Keldysh, *Zh. Eksp. Teor. Fiz.* **47**, 1945 (1965) [*Sov. Phys. JETP* **20**, 1307 (1965)].  
[18] X. M. Tong and S. I. Chu, *Chem. Phys.* **217**, 119 (1997).  
[19] X. M. Tong and S. I. Chu, *Phys. Rev. A* **61**, 021802 (2000).